


Research Article

Active Microvibration Control of Tool Platforms Installed on the Floors Subjected to Moving Vehicles in Industrial Factories

Chien-Liang Lee ¹, Yung-Tsang Chen,² Ray Kai Leung Su,³ and Yen-Po Wang⁴

¹School of Civil Engineering and Architecture, Xiamen University of Technology, Xiamen 361024, China

²Department of Civil Engineering, University of Nottingham Ningbo China, Ningbo 315100, China

³Department of Civil Engineering, The University of Hong Kong, Hong Kong, China

⁴Department of Civil Engineering, National Yang Ming Chiao Tung University, Hsinchu 300, Taiwan

Correspondence should be addressed to Chien-Liang Lee; leechienliang@xmut.edu.cn

Received 28 March 2023; Revised 26 September 2023; Accepted 5 October 2023; Published 27 October 2023

Academic Editor: Ka-Veng Yuen

Copyright © 2023 Chien-Liang Lee et al. This is an open access article distributed under the Creative Commons Attribution License, which permits unrestricted use, distribution, and reproduction in any medium, provided the original work is properly cited.

The vibration responses of tall flexible tool (or equipment) platforms subjected to floor excitations at the platform base are considered more crucial than those of the short ones. This study examined the microvibration control performance of the proposed active piezoelectric mass damper (APMD) or driver for tall platforms subjected to internal automated guided vehicle- (AGV-) induced floor vibrations with larger intensity and broader bandwidth in liquid-crystal-display (LCD) fabrication factories (fabs). The APMD did not require auxiliary spring and damping elements to tune the natural frequency and reduce the stroke of the mass block as required by typical active tuned mass dampers (ATMDs). The motion equation of the proposed analytical model including a continuous three-span beam (or floor) system and an active-controlled tool platform under the action of the AGV moving forces was derived. The APMD, consisting of piezoelectric stacks and a mass block, was installed on the platform subjected to the base rotation excitation, which could be attributed to the uneven vertical floor vibrations induced by AGVs. Moreover, the direct output feedback control algorithm was adopted to determine the optimal feedback gain matrix for calculating the active control force. Time history analyses of the continuous beam-platform model under different AGV weights moving at the same speed were performed, and the corresponding velocity vibration spectra of the floor and platform were further obtained through one-third octave band spectrum analysis. Numerical simulation results revealed that the microvibrations of the platform without APMD generally exceed the VC-A level regardless of the AGV weight. Significant reductions of over 90% on the platform microvibrations could be achieved after the platform was implemented with the APMD, and vibrations met the desired vibration limit (VC-B). Moreover, the APMD exhibits comparable microvibration control performance to the ATMD and requires less mass of the mass block, stroke, and applied voltage under the same active control force. In real-life high-tech production fabs, AGV-induced platform microvibrations occur all the time; therefore, the proposed APMD with less power consumption could be an economical and feasible approach for persistent microvibration control of tall platforms in LCD fabs.

1. Introduction

Microvibrations directly induced by internal automated material handling systems (AMHSs) [1], such as automated guided vehicles (AGVs) [2, 3], rail guided vehicles (RGVs), stockers (STKs) or moving cranes [4], and overhead hoist transfer (OHT) [5], on the production floors in semiconductor or liquid-crystal-display (LCD) fabrication factories (or fabs) have rarely been considered while designing

fab buildings. Consequently, majority of the AMHS-induced floor and platform vibrations surpass the allowable Bolt Beranek & Newman Vibration Criterion (BBN-VC) [6]. Figure 1 illustrates the process tools supported by tool platforms (or tool foundations) that are installed on the production floors in cleanrooms of high-tech fabs. The tool platforms are typically composed of steel material (e.g., steel beams, columns, and plates), with some being manufactured using concrete-infilled steel tubes. The short (or rigid)

platforms, lower than 1.0 m in height, are typically employed in semiconductor fabs, whereas the tall (or flexible) ones, higher than 2.0 m in height, are generally fabricated by the LCD fabs for manufacturing larger glass panels. The lateral stiffness of the tall platforms is substantially lower than that of the short ones such that their natural vibration frequencies generally lie within the bandwidth of the BBN-VC (4–100 Hz). Accordingly, the vibration response amplifications of the tall flexible platforms subjected to floor excitations at platform base are more remarkable than those of the short ones, and the vibration response on the platform top is larger than the allowable vibration limit within the required bandwidth. Additional horizontal vibration response on the top of the tall platforms can be attributed to the base rotation excitations induced from the uneven relative vertical floor vibrations generated by the moving AGVs. The taller the platform, the higher the microvibration level. Hence, the monitored vibration levels of tall platforms under the AGV moving loads in LCD fabs are substantially higher than the desired VC-B level or even the VC-A level. Here, VC-B denotes the vibration criterion- (VC-) B level. Furthermore, the VC curves are a set of allowable root mean square (RMS) velocity spectra (referred to as VC-A, VC-B, VC-C, VC-D, and VC-E) corresponding to the amplitude range of $50.8\text{--}3.175\ \mu\text{-m/s}$ ($0.0051\text{--}0.00032\ \text{cm/s}$) within a frequency range of 8–100 Hz.

The floor and platform microvibrations at precision high-tech fabs induced by external traffic such as nearby vehicles and trains have been extensively studied over the last two decades. Yang and Agrawal [7] proposed a hybrid floor isolation system with rubber bearings and actuators (electric or magnetostrictive) that were installed on the first floor of a three-story fab; they aimed to evaluate its control performance using the modified Kanai-Tajimi power spectral density (MKT-PSD) function to quantify the train-induced horizontal ground accelerations. Simulation results indicated that the root mean square (RMS) velocity spectrum of the hybrid floor isolation system satisfies VC-E if appropriate stiffness and damping of the hybrid floor isolation system are adopted. Xu et al. [8] established an analytical model considering a three-story fab building with a hybrid-controlled platform subjected to the train-induced vertical ground motion generated using a Fourier spectrum for a given distance from the track. The hybrid control platform consisted of active hydraulic actuators and passive mounts with springs and dashpots between the platform and building. Numerical results demonstrated that the vibration of the passive control platform may exceed VC-B, whereas that of the hybrid-controlled platform could be effectively suppressed to meet VC-E. Hong et al. [9] constructed a three-dimensional finite element building model with a hybrid platform subjected to three-dimensional ground excitations. The hybrid platform mounted on the second floor of the building consisted of several pairs of passive devices and active actuators. Numerical results demonstrated that the hybrid platform can effectively reduce the vibration responses in all directions to lie below VC-E.

Vibrations induced directly by the internal moving AMHs or trucks on the production floor in foundry fabs or

industrial factories have rarely been considered while designing the facilities. Pan et al. [10] investigated the container trucks traveling with varied speeds within the multistory factory buildings at the site of vibration-sensitive equipment installation. Moreover, the road roughness was considered and generated through a PSD function according to ISO 8606. Results demonstrated that the vertical floor vibrations induced by container trucks traveling at the speeds below 40 km/h generally meet the allowable vibration criterion. However, the peak vertical vibration may possibly exceed the more stringent vibration limit for certain extreme precision equipment (e.g., steppers). Hu et al. [5] proposed an analytical model including fab buildings with foundation, the OHT system, and the isolation system-controlled tool platform to investigate the OHT-induced floor microvibrations in semiconductor fabs. Results revealed that the predicted floor microvibrations are consistent with the in situ measurements beyond 10 Hz; however, they are underestimated below 10 Hz. Moreover, an 80% microvibration reduction for the isolated tool platform could be achieved. Ju et al. [4] constructed a realistic analytical model integrating a high-tech fab with waffle slabs, steel rails, and a crane to assess moving crane-induced floor microvibrations, and numerical results from finite element analysis agreed well with the experimental measurements. Moreover, they suggested that smoothing the wheel and rail, decreasing the speed of the crane, and increasing the slab and beam depths of the fab building are efficient in reducing floor microvibrations. Lee et al. [2, 3, 11] explored the AGV-induced floor microvibrations under different AGV moving conditions (e.g., weights and speeds) in LCD fabs. Moreover, fragility analysis was conducted to develop floor microvibration fragility surfaces that can be used to evaluate the exceedance probabilities of the preferred vibration level.

Piezoelectric actuators (PEAs) [12] have been widely employed as drivers or control units in precision positioning platforms, equipment, and civil structures owing to their specific advantages including compact size, high resolution, fast reaction time, low heat generation, low power consumption, and no electromagnetic interference (which is prohibited in high-tech fabs). Liu et al. [13] presented the recent advances in microvibration isolation in a state-of-the-art review paper and introduced various types of passive, active, semiactive, and hybrid isolation systems or devices implemented with piezoelectric materials or actuators. Song et al. [14] reviewed the vibration control of civil structures (e.g., beams, trusses, frames, and cable-stayed bridges) using piezoelectric patch or stack actuators. Kamada et al. [15] proposed an active control strategy for the flexural-shear type frame structures using the PEAs installed underneath the column bases. The installation locations of the PEAs can be appropriately managed to control the bending moments and axial forces of the columns. Experimental results of a four-story steel frame under the broader band random excitations indicated that the structural acceleration responses can be effectively reduced using the proposed control schemes. Hora et al. [16] proposed an active microvibration control system using PEAs to yield a reverse couple moment to suppress the vertical vibrations of the

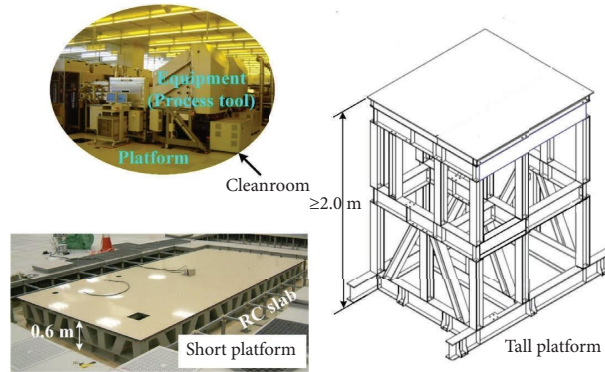


FIGURE 1: Process tools supported by the platforms installed on the production floors.

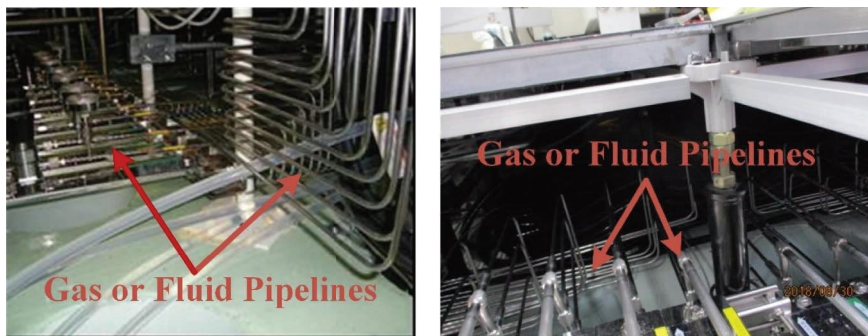


FIGURE 2: Gas or fluid supply pipelines connected between floors and processing tools.

floors in precision manufacturing factories simulated as a two-dimensional steel truss frame. The experimental results revealed that the floor acceleration response can be reduced to 1/32 of the noncontrolled case under the harmonic excitation. Etedali et al. [17] proposed a novel piezoelectric isolation system integrating an isolation system and piezoelectric friction dampers (PFDs) for seismic vibration control of isolated buildings. Using genetic algorithms, the optimal semiactive controllers can be obtained to generate the control forces of PFD. Simulation results of a benchmark five-story building demonstrated that the proposed PFD can reduce the seismic floor acceleration responses with less displacement demand of the base isolator under the cases of near- and far-field earthquakes. Fan et al. [18] explored the dynamic behavior of variable friction dampers using a piezoelectric ceramic tubular actuator simulated using ANSYS. A constitutive equation governing the force and displacement of the damper subjected to the harmonic load was proposed, and certain formulas for calculating the dissipated energy of the damper within one cycle were derived.

Vestad and Steinert [19] developed a simple flexible passive vibration isolation table (or mass block) suspended by four steel springs and connected by four viscous dampers. The natural frequency of the suspended table is 1.2 Hz (in the vertical direction), and it successfully mitigates vibration responses in the frequency range of 5–20 Hz, allowing vibration-sensitive experiments or high-resolution

measurements to be performed on the table. Yang et al. [20] investigated the dynamic behavior and vibration isolation of a flexible Stewart platform with six supporting legs consisting of flexible joints and uniaxial piezoelectric isolators. Moreover, a model-based decoupled controller was proposed to determine the active control force based on the leg's feedback force and position information. Both the simulation and experimental results demonstrated that the system's vibration isolation capabilities can be improved under vertical excitation generated by a shaker. Jiang et al. [21] proposed a three-degree-of-freedom stabilization platform that consists of three force-position integrated electric cylinders (or supporting legs) as active motion actuators. The platform was designed to adjust the stiffness of the cylinders to have good vertical vibration isolation performance and to keep the platform horizontally based on an adaptive active compliance control law. Simulation and experiment results indicated that the platform can perform well under a single-cylinder impact, three-dimensional disturbances, and irregular random excitations. Fang and Fang et al. [22–24] developed a series of passively damped outrigger systems for seismic vibration control of flexible high-rise buildings. The core of the high-rise building was simulated based on the cantilevered Timoshenko beam theory, and the viscous dampers were vertically implemented between outriggers and perimeter columns. Moreover, the authors also proposed optimization and genetic algorithms to determine the damper placement locations and corresponding parameters

to minimize structural responses, such as inter-story drifts and floor accelerations of high-rise buildings.

Most of the aforementioned flexible platforms were proposed primarily to support light-weight precision mechanical systems and metrology equipment in research laboratories; however, in real-life high-tech production fabs, there are several complicated pipelines connected between floors and heavy processing tools (or platforms) to supply gas and fluid materials (some are toxic) to processing tools for the manufacturing of wafers or glass panels, as shown in Figure 2. If isolation or supporting systems are to be installed underneath a heavy platform base for vibration isolation, higher control force demands are required, and numerous flexible pipeline joints or flexible connectors should be used to prevent pipeline damage due to relative displacements, which could be a challenging task. Therefore, microvibration control devices that can be installed on the top of specific tall production platforms, such as active tuned mass dampers (ATMDs), active mass drivers, or the proposed active piezoelectric mass damper (APMD), without requiring supplementary damping and spring elements to tune the natural frequency of the mass block, as will be introduced later, could be promising and practical alternatives.

Lin et al. [25] conducted the shaking table tests using a semiactive friction tuned mass damper (SAF-TMD) to assess its structural control performance under seismic excitation. The SAF-TMD can adjust the friction or clamping force provided by a PEA. Experimental results indicated that the control performance of the SAF-TMD is superior to that of the typical passive friction TMD under the same peak TMD stroke. Ju et al. [26] proposed a semiactive piezoelectric friction mass damper, the desired friction force of which can be adjusted from the input voltage command of PEAs. The performance of the damper was validated using a real-time hybrid testing method. Moreover, the other semiactive piezoelectric friction dampers developed for seismic vibration control of frame structures can be found in the literature [27–30].

The present study aimed to assess the active microvibration control performance of the equipment platform under the internal AGV movements in precision high-tech fabs. The motion equation of an analytical model including the three-span continuous beam (or floor) system and platform under the action of AGV moving loads (simulated using an MKT-PSD function [7, 31]) and active control force provided by a proposed active piezoelectric mass damper (APMD) was derived. Moreover, the direct output feedback control algorithm [32, 33] was adopted to determine the optimal feedback gain matrix for calculating the active control force. Dynamic time history analyses of the proposed model under different AGV weights moving at the same speed were further conducted using the state space

procedure (SSP) [34]. Moreover, the corresponding RMS floor and platform velocity vibration spectra were obtained via a one-third octave band spectrum analysis [35]. Finally, the control performance of the APMD and its required control demands such as the control force, stroke, and applied voltage were assessed and discussed.

2. Analytical Model of the Floor-Platform System under Moving Loads and Control Forces

Figure 3 illustrates the analytical model of the proposed floor-platform system under the AGV moving loads in LCD factories. The three-span continuous floor (or beam) system was simplified from a real LCD fab [11], and the platform with a width b and height h installed on the floor and implemented with the APMD (Figure 4) was modeled as a single-degree-of-freedom (SDOF) system subjected to the base rotation excitation and active control force. Notably, the rotation excitation at the platform base could be attributed to the uneven vertical floor vibrations under the AGV movements.

The displacement response in the vertical direction, $u(x, t)$, of a multispan continuous beam can be calculated from its modal displacements and the mode shape functions (i.e., the classical mode superposition method), as follows [36]:

$$u(x, t) = \sum_{i=1}^n \gamma_i(t) \psi_i(x), \quad (1)$$

where $\gamma_i(t)$ is the i -th modal coordinate, $\psi_i(x)$ is the i -th mode shape function, and n is the total number of vibrational modes to compute the vibration response.

Moreover, the linear equation of motion of the analytical model subjected to N moving concentrated axle loads (Figure 3) can be derived employing the Bernoulli–Euler beam theory without considering the shear deformation effect as follows [2, 3]:

$$\mathbf{M}\ddot{\boldsymbol{\gamma}}(t) + \mathbf{C}\dot{\boldsymbol{\gamma}}(t) + \mathbf{K}\boldsymbol{\gamma}(t) = \boldsymbol{\Psi}(t)\mathbf{L}(t), \quad (2)$$

where \mathbf{M} , \mathbf{C} , and \mathbf{K} represent the $n \times n$ mass, damping, and stiffness matrices, respectively; $\boldsymbol{\gamma}(t) = [\gamma_1(t) \ \gamma_2(t) \ \cdots \ \gamma_n(t)]^T$ denotes the $n \times 1$ modal displacement vector; $\boldsymbol{\Psi}(t) = \begin{bmatrix} \psi_1[x_1(t)] & \psi_1[x_2(t)] & \cdots & \psi_1[x_N(t)] \\ \psi_2[x_1(t)] & \psi_2[x_2(t)] & \cdots & \psi_2[x_N(t)] \\ \vdots & \vdots & \ddots & \vdots \\ \psi_n[x_1(t)] & \psi_n[x_2(t)] & \cdots & \psi_n[x_N(t)] \end{bmatrix}$ denotes the $n \times N$ location matrix of the moving axle loads on the beam; and $\mathbf{L}(t) = \{F_1(t) \ F_2(t) \ \cdots \ F_N(t)\}^T$ denotes the $N \times 1$ moving load vector. If the tall platform is mounted on the floor at locations between x_1 and x_2 (i.e., $b = x_2 - x_1$,

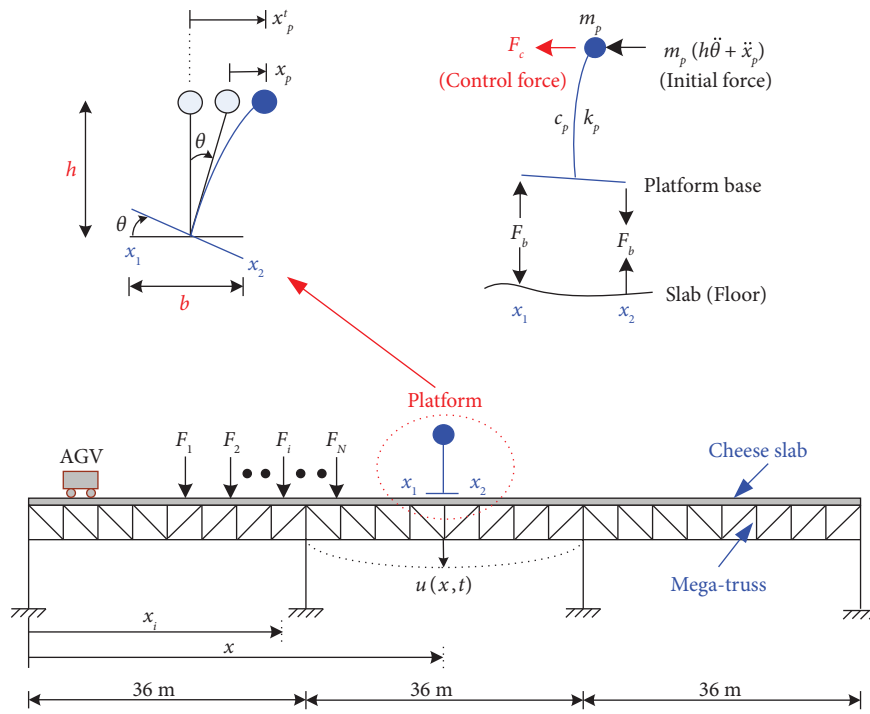


FIGURE 3: Analytical model of the floor-platform system under AGV moving loads in LCD factories.

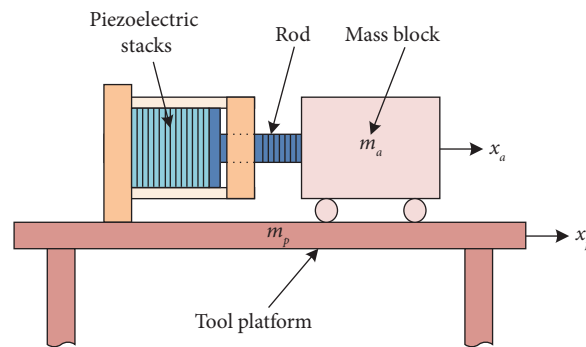


FIGURE 4: Schematic illustration of the proposed APMD installed on the tool platform.

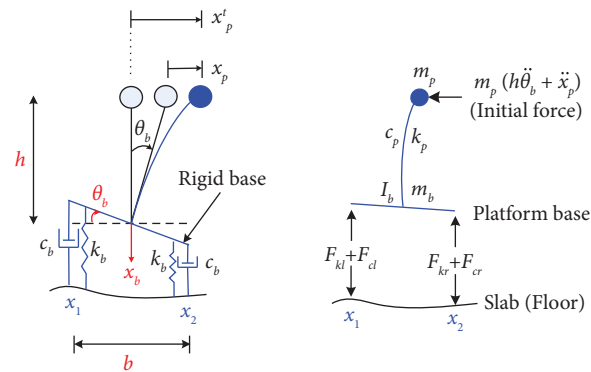


FIGURE 5: Analytical model of the platform implemented with passive base isolation system (two spring-dashpot models).

Figure 3), its equation of motion in the horizontal direction under the rotational base excitation ($\theta(t)$) and a single active

control force ($F_c(t)$, Figure 3) can be represented as follows [36]:

$$\begin{bmatrix} m_a & m_a \\ m_a & m_a + m_p \end{bmatrix} \begin{bmatrix} \ddot{x}_a(t) \\ \ddot{x}_p(t) \end{bmatrix} + \begin{bmatrix} c_a & 0 \\ 0 & c_p \end{bmatrix} \begin{bmatrix} \dot{x}_a(t) \\ \dot{x}_p(t) \end{bmatrix} + \begin{bmatrix} k_a & 0 \\ 0 & k_p \end{bmatrix} \begin{bmatrix} x_a(t) \\ x_p(t) \end{bmatrix} = - \begin{bmatrix} m_a \\ m_a + m_p \end{bmatrix} h \ddot{\theta}(t) + \begin{bmatrix} 1 \\ -1 \end{bmatrix} F_c(t), \quad (3)$$

where m_a , c_a , and k_a denote the system parameters (i.e., mass, damping, and stiffness, respectively) of the APMD; m_p , c_p , and k_p correspondingly represent the system parameters for the platform simulated as a SDOF system in this study; x_a represents the APMD stroke (displacement) of the mass block relative to the platform; x_p represents the displacement of the platform relative to the floor; and $F_c(t)$ represents the active control force provided by the piezoelectric stacks or actuators [12] (Figure 4) that can achieve the precision displacement control. The angular base acceleration can be further derived from the relative vertical floor accelerations at locations x_1 and x_2 as follows:

$$\begin{aligned} \ddot{\theta}(t) &= \frac{[\ddot{u}(x_2, t) - \ddot{u}(x_1, t)]}{b} \\ &= \frac{(\Psi_2^T - \Psi_1^T) \ddot{y}(t)}{b}, \end{aligned} \quad (4)$$

where $\Psi_1^T = \{\psi_1(x_1) \ \psi_2(x_1) \ \dots \ \psi_n(x_1)\}$ and $\Psi_2^T = \{\psi_1(x_2) \ \psi_2(x_2) \ \dots \ \psi_n(x_2)\}$ represent the row vectors that collect the mode shape values of each mode at locations x_1 and x_2 , respectively. Moreover, the base coupling force ($F_b(t)$) underneath the platform at x_1 and x_2 induced by the initial and active control forces can be derived using (4) as follows:

$$F_b(t) = m_p \ddot{x}_p(t) \frac{h}{b} + F_c(t) \frac{h}{b} = m_p [h \ddot{\theta}(t) + \ddot{x}_p(t)] \frac{h}{b} + F_c(t) \frac{h}{b} = \left[\frac{m_p h}{b} \ \frac{m_p h^2}{b^2} (\Psi_2^T - \Psi_1^T) \right] [\ddot{x}_p(t) \ddot{y}(t)] + F_c(t) \frac{h}{b}. \quad (5)$$

The modal coupling force ($F_b^*(t)$) exerted on the floor system at x_1 and x_2 can be represented as follows:

$$\begin{aligned} F_b^*(t) &= F_b(t) \Psi_1 - F_b(t) \Psi_2 \\ &= -(\Psi_2 - \Psi_1) \left[\frac{m_p h}{b} \ \frac{m_p h^2}{b^2} (\Psi_2^T - \Psi_1^T) \right] [\ddot{x}_p(t) \ddot{y}(t)] - (\Psi_2 - \Psi_1) F_c(t) \frac{h}{b} \\ &= \overline{\mathbf{M}} \{ \ddot{x}_p(t) \ddot{y}(t) \} - (\Psi_2 - \Psi_1) F_c(t) \frac{h}{b} \text{ where } \overline{\mathbf{M}} = -(\Psi_2 - \Psi_1) \left\{ \frac{m_p h}{b} \ \frac{m_p h^2}{b^2} (\Psi_2^T - \Psi_1^T) \right\}. \end{aligned} \quad (6)$$

The motion equation of the floor-platform system under the AGV moving loads and active control force can be represented using equations (2)–(4) and (6) as follows:

$$\begin{aligned}
& \left\{ \begin{bmatrix} m_a & m_a & \mathbf{0}_{1 \times n} \\ m_a & m_a + m_p & \mathbf{0}_{1 \times n} \\ \mathbf{0}_{n \times 1} & \mathbf{0}_{n \times 1} & \mathbf{M} \end{bmatrix} + \begin{bmatrix} 0 & 0 & \mathbf{0}_{1 \times n} \\ 0 & 0 & \frac{m_p h (\Psi_2^T - \Psi_1^T)}{b} \\ \mathbf{0}_{n \times 1} & \frac{m_p h (\Psi_2 - \Psi_1)}{b} & \frac{m_p h^2 (\Psi_2 - \Psi_1) (\Psi_2^T - \Psi_1^T)}{b^2} \end{bmatrix} \right\} [\ddot{x}_a(t) \ddot{x}_p(t) \ddot{\gamma}(t)] \\
& + \begin{bmatrix} c_a & 0 & \mathbf{0}_{1 \times n} \\ m_a & c_p & \mathbf{0}_{1 \times n} \\ \mathbf{0}_{n \times 1} & \mathbf{0}_{n \times 1} & \mathbf{C} \end{bmatrix} \begin{bmatrix} \dot{x}_a(t) \\ \dot{x}_p(t) \\ \dot{\gamma}(t) \end{bmatrix} + \begin{bmatrix} k_a & 0 & \mathbf{0}_{1 \times n} \\ m_a & k_p & \mathbf{0}_{1 \times n} \\ \mathbf{0}_{n \times 1} & \mathbf{0}_{n \times 1} & \mathbf{K} \end{bmatrix} \begin{bmatrix} x_a(t) \\ x_p(t) \\ \gamma(t) \end{bmatrix} = \begin{bmatrix} \mathbf{0}_{1 \times N} \\ \mathbf{0}_{1 \times N} \\ \Psi(t) \end{bmatrix} \mathbf{L}(t) + \begin{bmatrix} 1 \\ -1 \\ \frac{h(\Psi_2 - \Psi_1)}{b} \end{bmatrix} F_c(t) \\
& \implies \widehat{\mathbf{M}} [\ddot{x}_a(t) \ddot{x}_p(t) \ddot{\gamma}(t)] + \widehat{\mathbf{C}} \begin{bmatrix} \dot{x}_a(t) \\ \dot{x}_p(t) \\ \dot{\gamma}(t) \end{bmatrix} + \widehat{\mathbf{K}} \begin{bmatrix} x_a(t) \\ x_p(t) \\ \gamma(t) \end{bmatrix} = \mathbf{E}_c \mathbf{L}(t) + \mathbf{B}_c F_c(t),
\end{aligned} \tag{7}$$

where $\widehat{\mathbf{M}}$, $\widehat{\mathbf{C}}$, and $\widehat{\mathbf{K}}$ represent the $(n+2) \times (n+2)$ mass, damping, and stiffness matrices of the floor-platform system, respectively; \mathbf{E}_c represents the $(n+2) \times N$ location matrix of moving axle loads; and \mathbf{B}_c denotes the $(n+2) \times 1$ influence vector of the active control force, provided that only an APMD is considered in this study.

The dynamic vibration response or state $\mathbf{Z}[k] = \{ x_a[k] \ x_p[k] \ \gamma[k]^T \ \dot{x}_a[k] \ \dot{x}_p[k] \ \dot{\gamma}[k]^T \}^T$ including the displacement and velocity of the analytical model at each time step k for (7) can be recursively obtained using the SSP, as follows [33]:

$$\mathbf{Z}[k] = \mathbf{A}_d \mathbf{Z}[k-1] + (\mathbf{P}_1 + \mathbf{P}_2) (\mathbf{E}_c \mathbf{L}[k] + \mathbf{B}_c F_c[k]) - \mathbf{P}_2 (\mathbf{E}_c \mathbf{L}[k-1] + \mathbf{B}_c F_c[k-1]), \tag{8}$$

where $\mathbf{A}_d = \mathbf{I} + \mathbf{A}_c \varphi \Delta t$ represents the discrete-time system matrix, $\mathbf{A}_c = \begin{bmatrix} \mathbf{0} & \mathbf{I} \\ -\widehat{\mathbf{M}}^{-1} \widehat{\mathbf{K}} & -\widehat{\mathbf{M}}^{-1} \widehat{\mathbf{C}} \end{bmatrix}$ represents the continuous-time system matrix, $\mathbf{P}_1 = \varphi \Delta t$, $\mathbf{P}_2 = \mathbf{I} + \mathbf{A}_c \Delta t$, Δt represents the time interval, $\varphi = \mathbf{I} + \mathbf{A}_c \phi$, and $\phi = \Delta t/2 [\mathbf{I} + \mathbf{A}_c \Delta t/3 [\dots \mathbf{A}_c (\Delta t)/(s-1) [\mathbf{I} + \mathbf{A}_c \Delta t/s] \dots]]$ in which s denotes an integer value.

To further compare the control performance of tall flexible platforms using different control schemes, a passive base isolation system (PBIS) and typical ATMD were also investigated in this study. The tall platform controlled using the PBIS consisting of two spring-dashpot devices is illustrated in Figure 5. The equation of motion of the base-isolated platform supported by the floor under AGV moving loads can be derived as follows:

$$\begin{bmatrix} m_p & 0 & m_p h & \mathbf{0}_{1 \times n} \\ 0 & m_p + m_b & 0 & \mathbf{0}_{1 \times n} \\ m_p h & 0 & m_p h^2 + I_b & \mathbf{0}_{1 \times n} \\ \mathbf{0}_{n \times 1} & \mathbf{0}_{n \times 1} & \mathbf{0}_{n \times 1} & \mathbf{M} \end{bmatrix} \begin{bmatrix} \ddot{x}_p(t) \\ \ddot{x}_b(t) \\ \ddot{\theta}_b(t) \\ \dot{\gamma}(t) \end{bmatrix} + \begin{bmatrix} c_p & 0 & 0 & \mathbf{0}_{1 \times n} \\ 0 & 2c_b & 0 & -c_b(\Psi_2^T + \Psi_1^T) \\ 0 & 0 & \frac{c_b b^2}{2} & \frac{c_b b(\Psi_2^T - \Psi_1^T)}{2} \\ \mathbf{0}_{n \times 1} & -c_b(\Psi_2 + \Psi_1) & \frac{c_b b(\Psi_2 - \Psi_1)}{2} & \mathbf{C} + c_b(\Psi_2 \Psi_2^T + \Psi_1 \Psi_1^T) \end{bmatrix} \begin{bmatrix} \dot{x}_p(t) \\ \dot{x}_b(t) \\ \dot{\theta}_b(t) \\ \dot{\gamma}(t) \end{bmatrix} + \begin{bmatrix} k_p & 0 & 0 & \mathbf{0}_{1 \times n} \\ 0 & 2k_b & 0 & -k_b(\Psi_2^T + \Psi_1^T) \\ 0 & 0 & \frac{k_b b^2}{2} & \frac{k_b b(\Psi_2^T - \Psi_1^T)}{2} \\ \mathbf{0}_{n \times 1} & -k_b(\Psi_2 + \Psi_1) & \frac{k_b b(\Psi_2 - \Psi_1)}{2} & \mathbf{K} + k_b(\Psi_2 \Psi_2^T + \Psi_1 \Psi_1^T) \end{bmatrix} \begin{bmatrix} x_p(t) \\ x_b(t) \\ \theta_b(t) \\ \gamma(t) \end{bmatrix} = \begin{bmatrix} \mathbf{0}_{1 \times N} \\ \mathbf{0}_{1 \times N} \\ \mathbf{0}_{1 \times N} \\ \Psi(t) \end{bmatrix} \mathbf{L}(t), \quad (9)$$

where m_b and I_b denote the mass and moment of inertia of the rigid platform base, respectively; c_b and k_b denote the damping and stiffness coefficients of the base isolation system (two spring-dashpot model), respectively; and x_b and θ_b denote the vertical displacement (measured from the position of static equilibrium) and angular rotation of the rigid platform base, respectively. Moreover, the spring and damping forces can be represented as $F_{kl}(t) = k_b \{x_b(t) - u(x_1, t) + [b\theta_b(t)]/2\}$ (or $F_{kr}(t) = k_b \{x_b(t) - u(x_2, t) - [b\theta_b(t)]/2\}$) and $F_{cl}(t) = c_b \{\dot{x}_b(t) - \dot{u}(x_1, t) + [b\dot{\theta}_b(t)]/2\}$ (or $F_{cr}(t) = c_b \{\dot{x}_b(t) - \dot{u}(x_2, t) - [b\dot{\theta}_b(t)]/2\}$), respectively. The stiffness coefficient of the base isolation system was defined and determined by a given frequency, f_b , as $k_b = (m_p + m_b) \times (2\pi f_b)^2$. Similarly, the damping coefficient of the base isolation system was determined by a given damping ratio, ξ_b , as $c_b = 2 \times (m_p + m_b) \times (2\pi f_b) \times \xi_b$.

3. Direct Output Feedback Control Algorithm

The present study adopted the direct output feedback control algorithm [32, 33] to determine the optimal feedback gain matrix and compute the control force using only the partial output state responses ($\mathbf{y}[k]$), which can be represented as follows:

$$F_c(t) = \mathbf{G}\mathbf{y}[k] = \mathbf{G}\mathbf{D}\mathbf{Z}[k], \quad (10)$$

where $\mathbf{y}[k]$ represents the $r \times 1$ output state vector (if the number of the output state response is r , $r \leq 2(n+2)$), \mathbf{G} represents the $r \times r$ feedback gain matrix, and \mathbf{D} represents the $r \times 2(n+2)$ location matrix of the output state. Herein, we only considered the velocity response of the platform (i.e., $r = 1$ and $\mathbf{D} = [0 \ 0 \ \mathbf{0}_{1 \times n} \ 0 \ 1 \ \mathbf{0}_{1 \times n}]$) as the output state. The performance index, $J[k]$, for each time instant k can be defined as follows:

$$J[k] = \mathbf{Z}^T[k] \mathbf{Q} \mathbf{Z}[k] + F_c^T[k] \mathbf{R} F_c[k], \quad (11)$$

where an optimal solution exists only if the weighting matrices (or scalars) \mathbf{Q} and \mathbf{R} are semipositive and positive definites, respectively. Herein, the weighting matrix $\mathbf{Q} = \begin{bmatrix} k_p & \mathbf{0} \\ \mathbf{0} & m_p \end{bmatrix}$ was adopted to reserve the first term on the R.H.S. of (11) as the total strain and kinetic energy of the platform. \mathbf{R} is a scalar quantity, as only a single APMD was considered. Hence, the optimal feedback gain matrix, \mathbf{G} (or gain factor G for single output response), can be obtained using the equation as follows [33]:

$$\frac{dJ[k]}{d\mathbf{G}} = \mathbf{0} \Rightarrow \mathbf{G} = -\mathbf{R}^{-1} \mathbf{B}_1^T (\mathbf{I} - \mathbf{B}_1 \mathbf{G} \mathbf{D})^{-T} (\mathbf{Q} + \mathbf{D}^T \mathbf{G}^T \mathbf{R} \mathbf{G} \mathbf{D}) (\mathbf{I} - \mathbf{B}_1 \mathbf{G} \mathbf{D})^{-1} (\mathbf{I} - \mathbf{B}_1 \mathbf{G} \mathbf{D})^{-T} \mathbf{D}^T \cdot [\mathbf{D} (\mathbf{I} - \mathbf{B}_1 \mathbf{G} \mathbf{D})^{-1} (\mathbf{I} - \mathbf{B}_1 \mathbf{G} \mathbf{D})^{-T} \mathbf{D}^T]^{-1} \text{ where } \mathbf{B}_1 = (\mathbf{P}_1 + \mathbf{P}_2) \mathbf{B}_c. \quad (12)$$

The optimal gain matrix (\mathbf{G}) shown in (12) is represented implicitly and can be determined using an iterative method as follows [32, 33]:

$$\begin{aligned} \bar{\mathbf{G}}^{(i)} = & -\mathbf{R}^{-1}\mathbf{B}_1^T(\mathbf{I} - \mathbf{B}_1\mathbf{G}^{(i)}\mathbf{D})^{-T} \left(\mathbf{Q} + \mathbf{D}^T\mathbf{G}^{(i)T}\mathbf{R}\mathbf{G}^{(i)}\mathbf{D} \right) (\mathbf{I} - \mathbf{B}_1\mathbf{G}^{(i)}\mathbf{D})^{-1} (\mathbf{I} - \mathbf{B}_1\mathbf{G}^{(i)}\mathbf{D})^{-T} \mathbf{D}^T \\ & \cdot \left[\mathbf{D}(\mathbf{I} - \mathbf{B}_1\mathbf{G}^{(i)}\mathbf{D})^{-1} (\mathbf{I} - \mathbf{B}_1\mathbf{G}^{(i)}\mathbf{D})^{-T} \mathbf{D}^T \right]^{-1}, \end{aligned} \quad (13)$$

- (3) Consider $\mathbf{G}^{(i+1)} = (\mathbf{G}^{(i)} + \lambda\bar{\mathbf{G}}^{(i)})/(1 + \lambda)$, where λ denotes a step factor. The smaller the factor, the slower the convergence, with a better numerical stability.
- (4) Stop if $|\mathbf{G}^{(i+1)} - \mathbf{G}^{(i)}| \leq \varepsilon$, where ε denotes the tolerance of error; otherwise, consider $i = i + 1$ and $\mathbf{G}^{(i)} = \mathbf{G}^{(i+1)}$ and repeat since step (2).

4. Assessment of AGV-Induced Floor and Platform Microvibrations

4.1. Target LCD Fab Model. Figure 3 illustrates a three-span typical LCD fab [11] with a long span (36 m) mega truss floor system under AGV movements. The mass per unit length and flexural rigidity of the beam model are 9.1505×10^3 kg/m and

- (1) Consider $i = 1$ and $\mathbf{G}^{(i)} = \mathbf{0}$.
- (2) Substitute $\mathbf{G}^{(i)} = \mathbf{0}$ into equation (12), yielding

2.4608×10^{11} N-m², respectively; accordingly, the eigenanalysis yielded the first five vibration frequencies of the continuous beam model as follows: 6.285, 8.055, 11.762, 25.142, and 28.653 Hz, respectively. Notably, the total number of vibrational modes, $n = 12$, was considered to compute the vibration response of the floor system. Moreover, an equivalent damping ratio of 5% was assigned to each vibration mode.

4.2. Simulation of AGV Moving Forces. Herein, a single AGV with two equal axle loads ($N = 2$) was assumed to traverse the floor system. The AGV moving force (or dynamic engine force) can be obtained using an MKT-PSD function or spectrum [7, 31] given by the following expression:

$$F(f) = \frac{[1 + 4\xi_1^2(f/f_1)^2](f/f_2)^2 S_0}{\left\{ [1 - (f/f_1)^2]^2 + 4\xi_1^2(f/f_1)^2 \right\} \left\{ [1 - (f/f_2)^2]^2 + 4\xi_2^2(f/f_2)^2 \right\}}, \quad (14)$$

where f_1 , f_2 , ξ_1 , and ξ_2 denote the constant parameters; f_1 and f_2 represent the maximum and minimum frequencies of the predominant bandwidth of the moving force, respectively; ξ_1 and ξ_2 control the configuration of the PSD functions; and S_0 denotes the magnitude of the force. To investigate the effects of the AGV weight on the floor and platform microvibrations, five different AGV weights with $w_5 = 21582$ N (i.e., the maximum AGV weight equivalent to the mass of 2200 kg), $w_4 = 0.8w_5$, $w_3 = 0.6w_5$, $w_2 = 0.4w_5$, and $w_1 = 0.2w_5$ were considered for the time history analysis. Notably, the AGVs herein were moving at $v = 2.0$ m/s. Figure 6 demonstrates the dynamic engine force MKT-PSD spectra of the five AGV weights, and their corresponding governing parameters with $f_1 = 50$ Hz are listed in Table 1. The intensity and frequency bandwidth of the MKT-PSD functions vary and increase with increasing AGV weights. These calibrated moving force PSD spectra can be obtained using the previously reported regression formulas [31]. Moreover, the PSD spectra were further transformed into dynamic engine force time histories [37], as shown in Figure 6, for conducting the dynamic time history analyses. The maximum force of each axle of the AGV for $w_5 = 21582$ N and $v = 2.0$ m/s was scaled to be 2453 N (i.e., approximately 11.4% of the AGV weight or

equivalent to a mass of 250 kg) to better predict the in situ microvibration level as suggested by Lee et al. [11].

4.3. Parameters of the Platform and Piezoelectric Actuator. The horizontal natural frequency and equivalent damping ratio of the 3000 kg platform installed at central location of midspan ($x = 54$ m) were 25 Hz and 2%, respectively. Moreover, the width (b) and height (h) of the platform were 2.0 and 2.6 m, respectively. The cross-sectional area (A_d) of the piezoelectric stack actuator was 5.07 cm² (equivalent to the diameter of 2.54 cm), total number of layers (n_d) of piezoelectric material was 200, thickness (t_d) of each layer was 0.051 cm, and piezoelectric strain constant (d_{33}) and the modulus of elasticity (E_d) of the piezoelectric material were 3.71×10^{-10} (m/V) and 4.62×10^7 kN/m², respectively [30]. Moreover, the mass (m_a) of the APMD mass block was 50 kg, and the damping (c_a) and stiffness (k_a) of the APMD were assumed to be 0.

4.4. Microvibration Simulation Results. Figure 7 presents the simulated vertical RMS floor velocity spectra at central location of the midspan ($x = 54$ m) under different AGV weights. The floor vibrations increased with increasing AGV

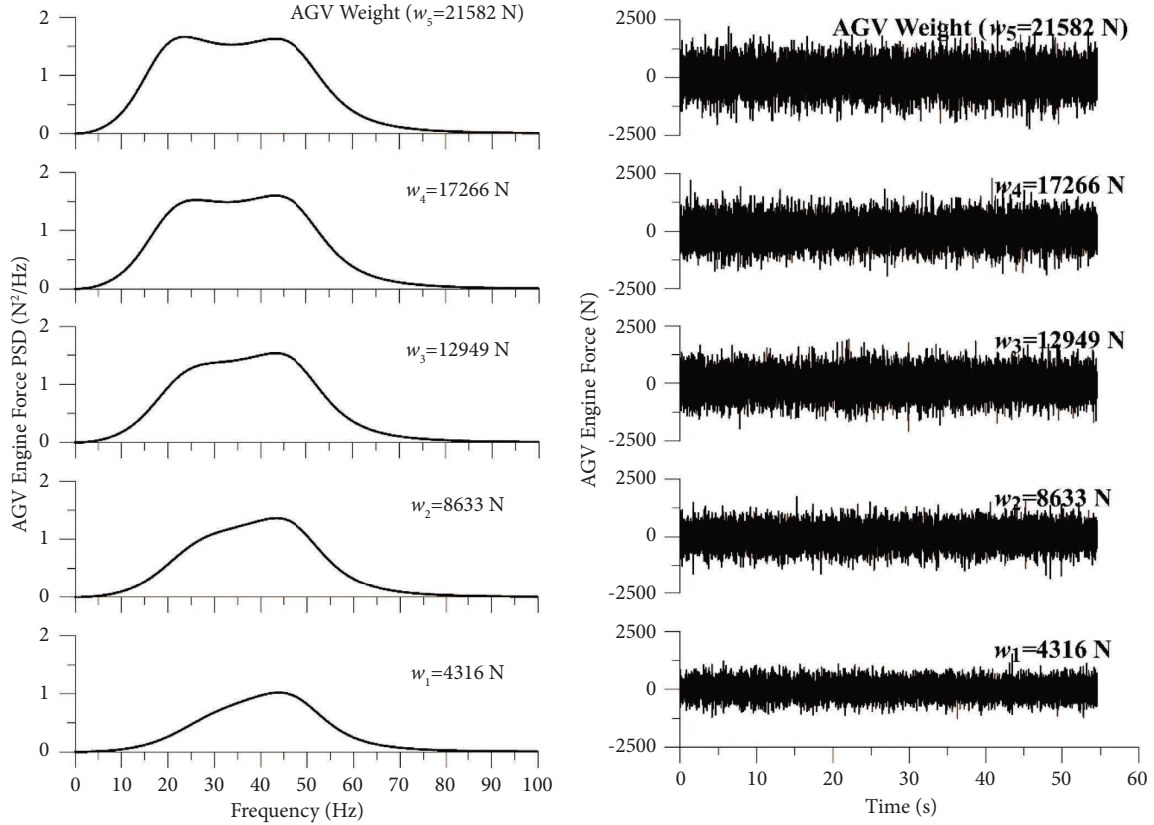


FIGURE 6: Dynamic engine force PSDs and time histories of each axle under different AGV weights.

TABLE 1: Parameters of the simulated MKT-PSD functions for different AGV weights.

| AGV weight | f_1 (Hz) | f_2 (Hz) | ξ_1 | ξ_2 | S_0 ($N \cdot s^{1/2}$) |
|------------|------------|------------|---------|---------|-----------------------------|
| w_5 | 50 | 20.5250 | 0.23 | 0.51 | 1.0758 |
| w_4 | 50 | 21.7678 | 0.23 | 0.51 | 0.9969 |
| w_3 | 50 | 23.7082 | 0.23 | 0.51 | 0.8855 |
| w_2 | 50 | 26.3462 | 0.23 | 0.51 | 0.7415 |
| w_1 | 50 | 29.6818 | 0.23 | 0.51 | 0.5650 |

weight. For example, the floor vibration could exceed VC-A for the maximum AGV weight (w_5), whereas they could reach VC-B for the minimum AGV weight (w_1). Moreover, the acceleration time histories and their corresponding RMS velocity spectra of the platform without control, shown in Figures 8 and 9, respectively, substantially exceeded VC-A at approximately 25 Hz (i.e., the fundamental frequency of the platform) regardless of the weight of AGV. These results indicate that the AGV-induced floor and platform vibrations generally exceed the allowable VC-B level required by the LCD factory.

Figures 8 and 9 demonstrating the comparisons of the platform vibrations without and with APMD ($m_a = 50$ kg and $R = 10^{-8.5}$) indicate the achievement of significant reductions (over 90%) on the platform responses in both the time and frequency domains. They further indicate that the platform vibrations were effectively suppressed to satisfy the desired VC-B level after implemented with the APMD.

Figures 10–13 demonstrate the simulated time histories of the active control force, applied voltage, stroke of mass block, and power demand of the APMD, respectively. The relationship between the stroke ($x_a(t)$) of the mass block (or the deformation of the piezoelectric stacks) and active control force ($F_c(t)$) of the piezoelectric stacks can be represented as follows [30]:

$$\begin{aligned}
 F_c(t) &= \frac{E_d A_d}{n_d t_d} [n_d d_{33} V(t) - x_a(t)] \\
 &= k_d [n_d d_{33} V(t) - x_a(t)],
 \end{aligned} \tag{15}$$

where $k_d = (E_d A_d) / (n_d t_d)$ is the stiffness of the piezoelectric stacks in the polarization direction (axial direction) and $V(t)$ represents the applied voltage. Using the control force and stroke of the mass block, the corresponding applied voltage command of the APMD can be determined using (15) as follows:

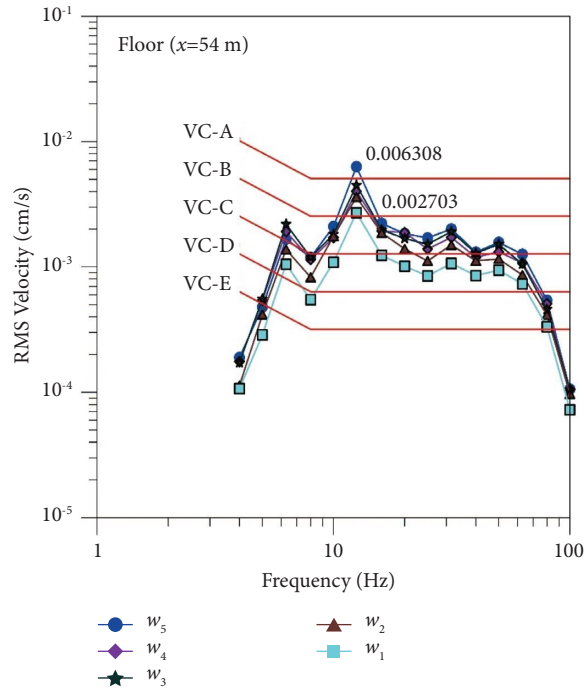


FIGURE 7: RMS floor vibration spectra at central location of the midspan under different AGV weights.

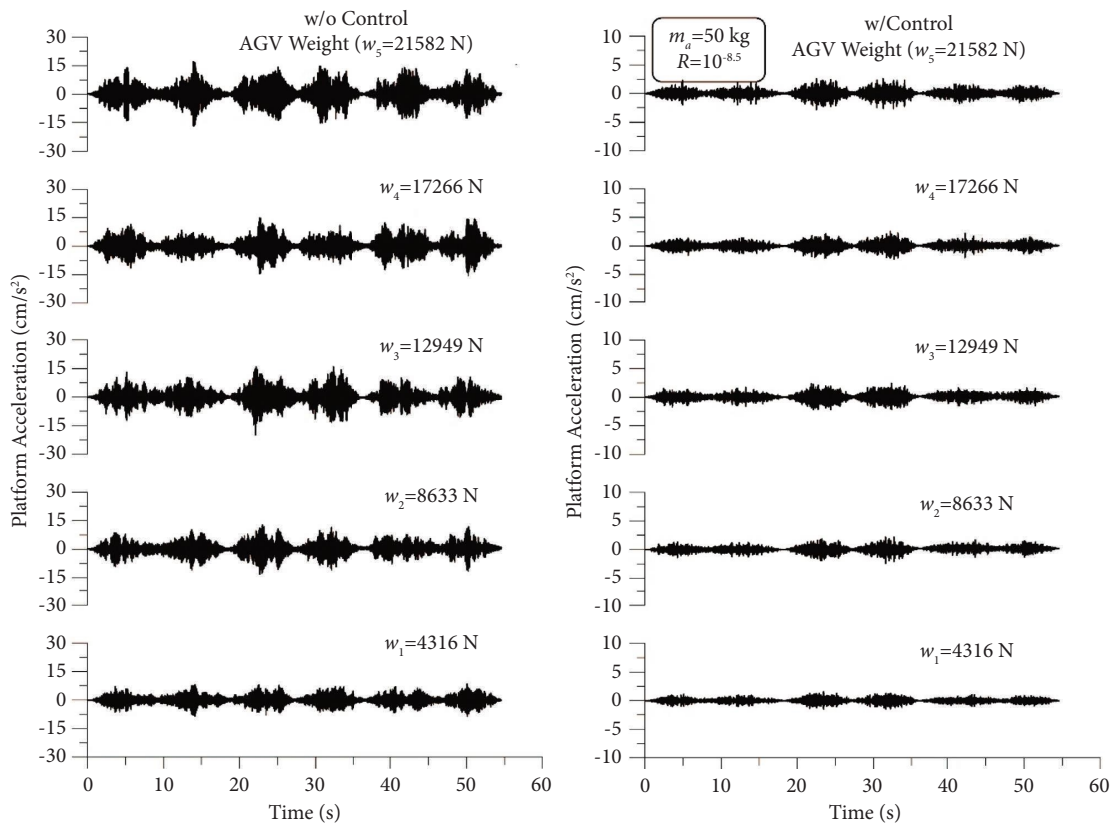


FIGURE 8: Acceleration time histories of the platform with and without APMD under different AGV weights (mass of the mass block $m_a = 50$ kg; active control force weighting factor $R = 10^{-8.5}$).

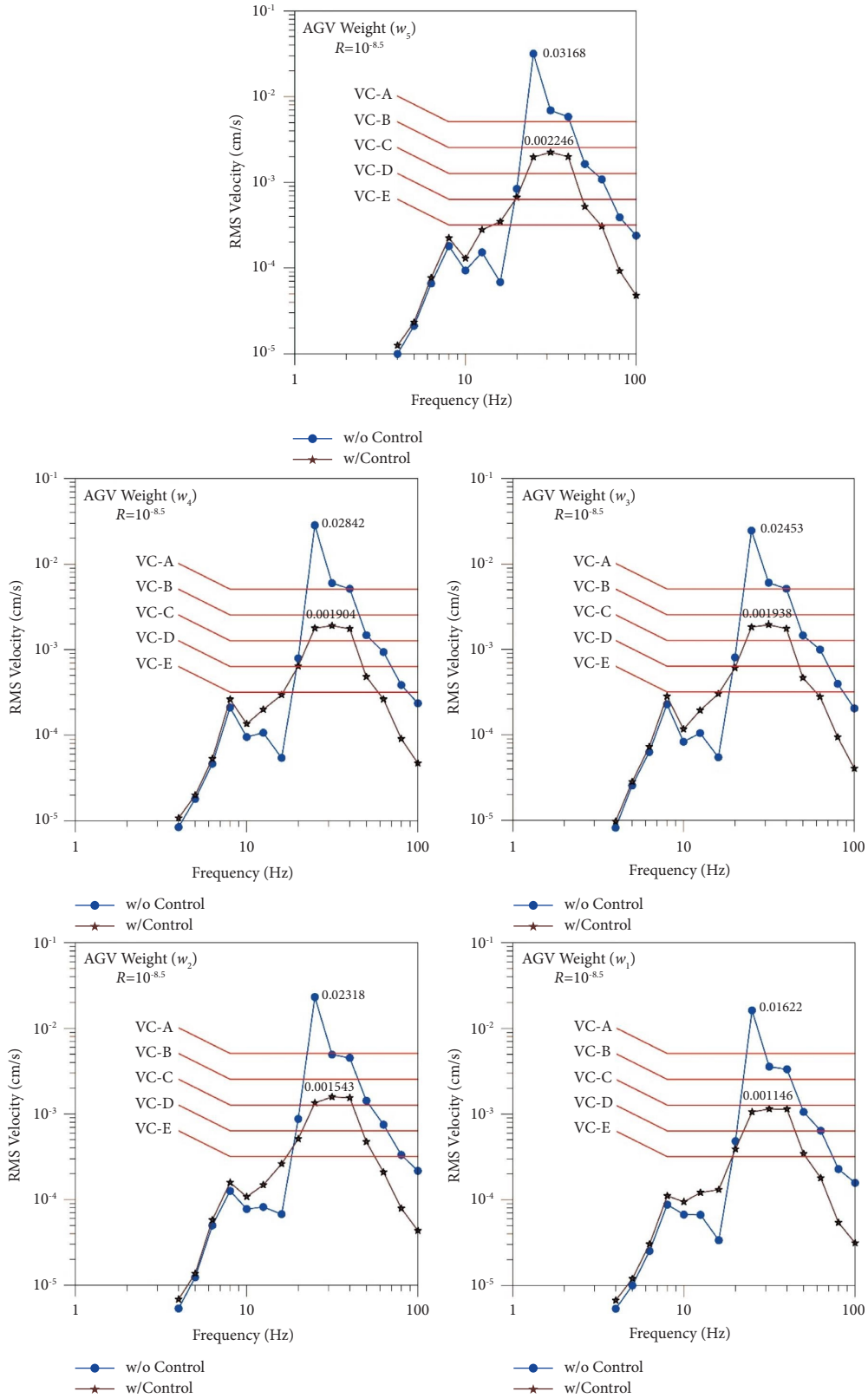


FIGURE 9: RMS vibration spectra of the platform with and without APMD under different AGV weights (mass of the mass block $m_a = 50$ kg; active control force weighting factor $R = 10^{-8.5}$).

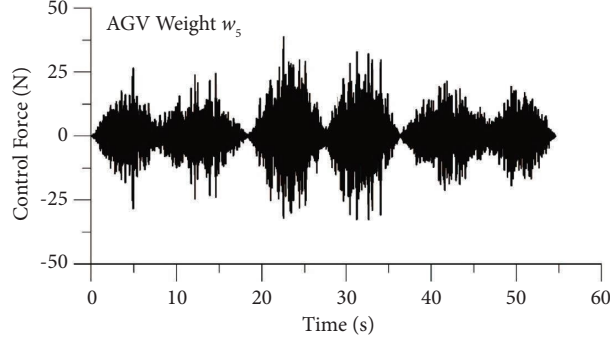


FIGURE 10: Control force time history of the APMD under the maximum AGV weight (mass of the mass block $m_a = 50$ kg; active control force weighting factor $R = 10^{-8.5}$).

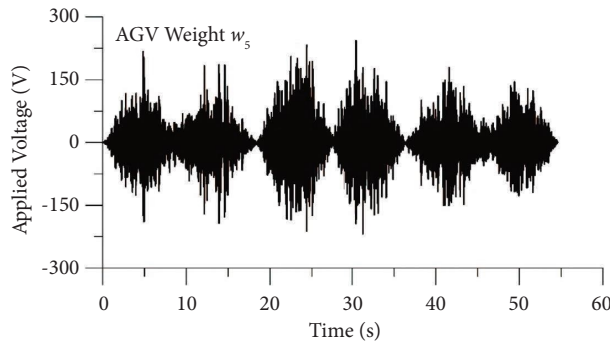


FIGURE 11: Applied voltage time history of the APMD under the maximum AGV weight (mass of the mass block $m_a = 50$ kg; active control force weighting factor $R = 10^{-8.5}$).

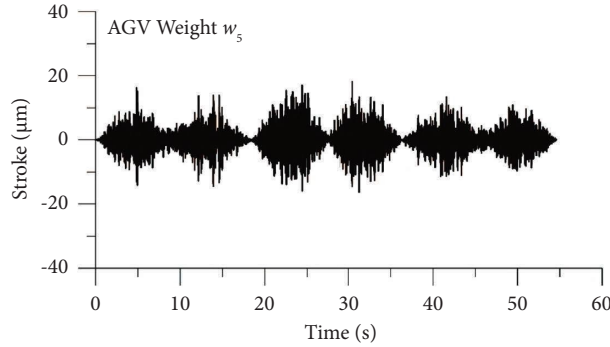


FIGURE 12: Stroke time history of the APMD under the maximum AGV weight (mass of the mass block $m_a = 50$ kg; active control force weighting factor $R = 10^{-8.5}$).

$$V(t) = [F_c(t) + k_a \dot{x}_a(t)] / (n_d d_{33} k_d). \quad (16)$$

Moreover, the power demand of the APMD can be calculated using the control force and velocity of the mass block as follows:

$$P(t) = F_c(t) \dot{x}_a(t). \quad (17)$$

To explore the effect of the weighting factor (R) of the active control force on the performance of the APMD, the weighting factors between $R = 10^{-5}$ and $R = 10^{-8.5}$ were

considered in this study. As presented in Table 2, the smaller the R value, the larger the feedback gain factor and the corresponding active control force. Notably, the feedback gain factors were obtained using the step factor $\lambda = 0.01$ and tolerance of error $\varepsilon = 10^{-7}$. Moreover, the maximum control force, applied voltage, stroke, and power demands of the APMD with $m_a = 50$ kg and different R values simulated from the time history analyses under different AGV weights are summarized in Table 2. The maximum control demands of APMD increase with decreasing R values. Moreover, the APMD demonstrates the control performance only if the R

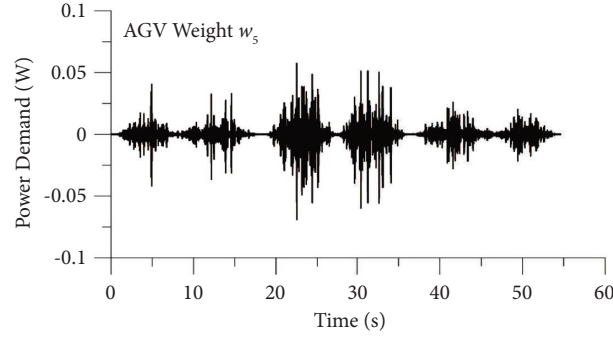


FIGURE 13: Power demand time history of the APMD under the maximum AGV weight (mass of the mass block $m_a = 50$ kg; active control force weighting factor $R = 10^{-8.5}$).

value meets the condition of $R \leq 10^{-8}$, within which the APMD can provide considerable active control force to suppress the AGV-induced platform microvibrations. The satisfactory control performance, as shown in Figures 8 and 9 ($m_a = 50$ kg), can be achieved at $R = 10^{-8.5}$ (corresponding to $G = 318915.02$). For example, for the maximum AGV weight (w_5), the platform microvibration can be effectively controlled to be below the allowable VC-B level at the maximum active control force of only 38.74 N, applied voltage of 242.99 V, stroke of 18.16 μm , and power of 0.069 Watt (W), as illustrated in Figures 10–13, respectively. Compared to the application of the PEAs in structural vibration control of civil structures under earthquake or wind excitations, the application of the proposed APMD with relatively smaller control demands is feasible for microvibration control of tall platforms in LCD fabs, as suggested by the simulated results in this study.

For better understanding the effect of the mass block on control demands of the APMD, different masses of the mass block are further considered for dynamic time history analyses. Figures 14–16 demonstrate the maximum stroke, applied voltage, and power demands with the varying mass of the APMD (10–100 kg) and the active control force weighting factor ($10^{-8.5}$ – 10^{-5}), provided that the optimal active control force time history has been obtained as shown in Figure 10. The results indicate that the peak control demands decrease with increasing APMD mass and decreasing active control force weighting factor. If the appropriate mass block, say $m_a \geq 50$ kg (equivalent to approximately 1.7% of the total weight of the platform), and the weighting factor of $R = 10^{-8.5}$ (or $R \leq 10^{-8}$) are adopted, the APMD can also achieve a satisfactory vibration control performance requiring less and more reasonable control demands than those summarized in Table 2 for $m_a = 50$ kg. Regarding the mechanisms of the APMD, the reaction force from the mass block of the APMD is considered as the active control force exerted to the tall platform. Unlike typical ATMD systems, the APMD did not require tuning its natural frequency in resonance with the horizontal frequency (25 Hz) of the tall platform such that the APMD could require less stroke of the mass block to achieve satisfactory vibration control performance. In addition, under the same active control force or energy demands, the larger the mass of the mass block, the smaller the corresponding stroke of the mass block (or the

piezoelectric stack actuator), applied voltage, and power demand. Therefore, the mass of the mass block can be easily selected based on the available installation space and the desired capacities of the stroke and applied voltage of the piezoelectric stack actuator from (15) and (16). Furthermore, unlike typical seismic active control systems that are operational for only dozens of seconds with larger control force or external energy for suppressing earthquake-induced structural vibrations, the APMD used for mitigating platform microvibrations induced by AGVs in real-life high-tech production fabs is operational all the time and requires less power consumption, as depicted in Figure 13 and Table 2. The proposed APMD driven by piezoelectric stack actuators has a high precision control capability. It provides a preliminary economical solution and demonstrates the potential for facilitating persistent microvibration control of special taller platforms subjected to such AGV-induced platform base rotation excitations with larger intensity and broader bandwidth in LCD fabs or similar industrial factories.

Moreover, the control performance of tall flexible platforms using different control schemes, a passive base isolation system (PBIS), and typical ATMD was also investigated in this study. The different frequency parameters ($f_b = 10, 30,$ and 50 Hz) and the damping ratio parameter ($\xi_b = 10\%$), along with $m_b = 300$ kg and $I_b = 100$ kg \cdot m², were considered in this study to evaluate the vibration isolation performance of the PBIS for the tall flexible platform. In addition, the typical ATMD considered in this study consists of an actuator, a mass block ($m_a = 150$ kg), a damping element with an equivalent damping ratio (ξ_{atmd}) of 20%, and a spring element with an equivalent frequency (f_{atmd}) of 25 Hz (i.e., equal to the horizontal natural frequency of the tall platform). Moreover, the optimal feedback gain factor of the ATMD was found to be $G = 318804.88$, using the same direct output feedback gain algorithm with $R = 10^{-8.5}$ and the same feedback output state being the velocity response of the tall platform as considered by the APMD.

Figure 17 shows a comparison of horizontal RMS vibration spectra of the tall platform implemented with APMD, ATMD, or PBIS under the maximum AGV weight. The simulated results show that all three control or isolation approaches considered in this study can suppress the horizontal microvibrations of the tall

TABLE 2: Summary of the feedback gain factors and corresponding maximum control demands of APMD for different active control force weighting factors R ($m_a = 50$ kg).

| Weighting factor (R) | 10^{-5} | 10^{-6} | 10^{-7} | 10^{-8} | $10^{-8.5}$ |
|------------------------------------------------|-----------|-----------|-----------|-----------|-------------|
| Feedback gain factor (G) | 100.85 | 1008.50 | 10084.98 | 100849.78 | 318915.02 |
| <i>AGV weight ($w_5 = 21582$ N)</i> | | | | | |
| Maximum control force (N) | 0.08 | 0.73 | 5.52 | 21.79 | 38.74 |
| Maximum voltage (V) | 62.61 | 60.66 | 69.86 | 173.33 | 242.99 |
| Maximum stroke (μm) | 4.65 | 4.50 | 5.20 | 12.95 | 18.16 |
| Maximum power (W) | <0.001 | <0.001 | 0.0038 | 0.0263 | 0.0690 |
| <i>AGV weight ($w_4 = 0.8w_5$)</i> | | | | | |
| Maximum control force (N) | 0.07 | 0.72 | 4.97 | 18.03 | 30.45 |
| Maximum voltage (V) | 65.79 | 64.00 | 73.13 | 158.40 | 191.41 |
| Maximum stroke (μm) | 4.88 | 4.75 | 5.44 | 11.83 | 14.35 |
| Maximum power (W) | <0.001 | <0.001 | 0.0037 | 0.0191 | 0.0485 |
| <i>AGV weight ($w_3 = 0.6w_5$)</i> | | | | | |
| Maximum control force (N) | 0.09 | 0.82 | 5.99 | 20.36 | 31.21 |
| Maximum voltage (V) | 68.64 | 66.63 | 74.22 | 179.39 | 212.87 |
| Maximum stroke (μm) | 5.09 | 4.94 | 5.53 | 13.40 | 15.91 |
| Maximum power (W) | <0.001 | <0.001 | 0.0043 | 0.0249 | 0.0448 |
| <i>AGV weight ($w_2 = 0.4w_5$)</i> | | | | | |
| Maximum control force (N) | 0.05 | 0.51 | 3.66 | 19.69 | 31.33 |
| Maximum voltage (V) | 43.41 | 41.96 | 46.44 | 147.68 | 216.25 |
| Maximum stroke (μm) | 3.22 | 3.11 | 3.46 | 11.04 | 16.18 |
| Maximum power (W) | <0.001 | <0.001 | 0.0017 | 0.0210 | 0.0469 |
| <i>AGV weight ($w_1 = 0.2w_5$)</i> | | | | | |
| Maximum control force (N) | 0.04 | 0.38 | 2.93 | 11.47 | 19.13 |
| Maximum voltage (V) | 32.42 | 31.84 | 38.91 | 94.78 | 109.65 |
| Maximum stroke (μm) | 2.41 | 2.36 | 2.90 | 7.07 | 8.20 |
| Maximum power (W) | <0.001 | <0.001 | 0.0012 | 0.0066 | 0.0182 |

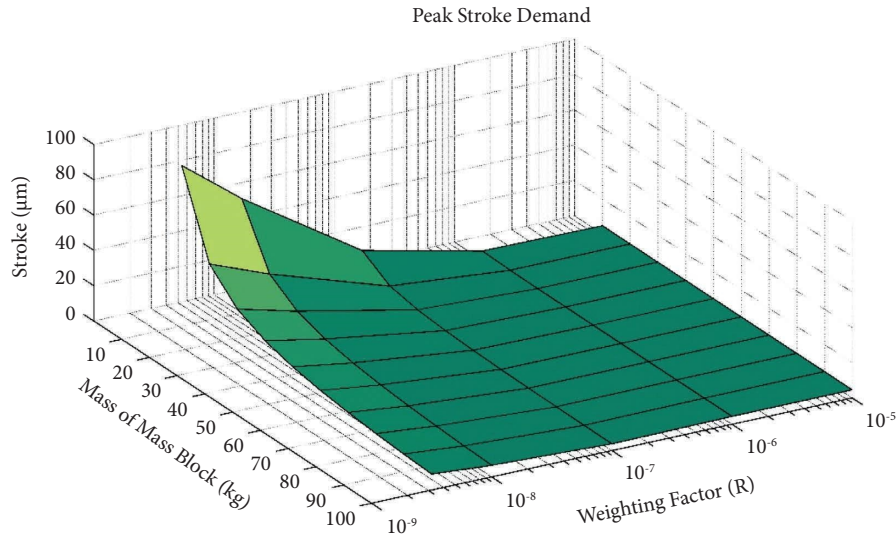


FIGURE 14: Peak stroke demands with different masses of mass block and active control force weighting factor under the maximum AGV weight.

platform below the allowable VC-B level if proper control system design parameters are adopted. The APMD with mass (m_a) of the mass block of 50 kg, peak active control force (F_c) of 38.74 N, and stroke (x_a) of 18.16 μm exhibits comparable control performance to the ATMD requiring

almost the same control force, $F_c = 39.66$ N; however, the ATMD should be designed using larger mass ($m_a = 150$ kg) of the mass block and higher damping ($\xi_{\text{atmd}} = 20\%$) to achieve the aforementioned satisfactory performance and realize a smaller stroke demand,

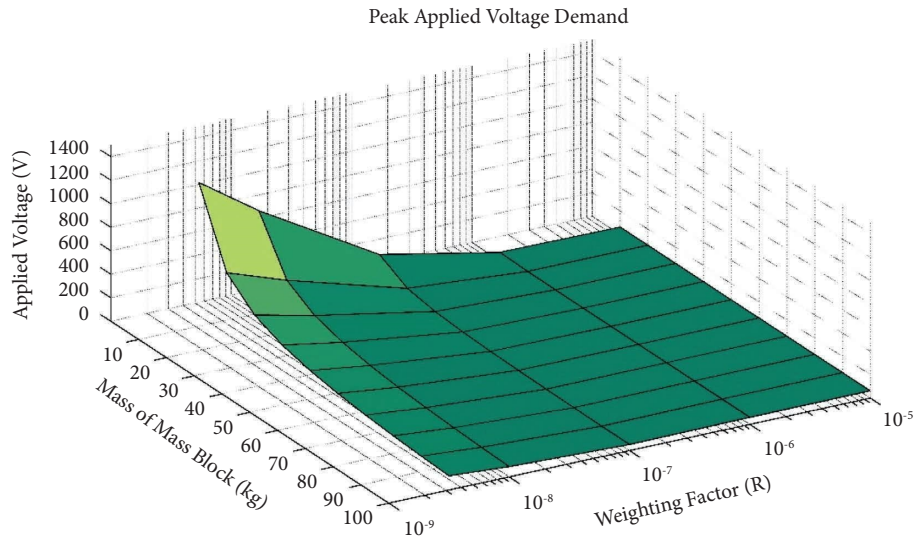


FIGURE 15: Peak applied voltage demands with different masses of mass block and active control force weighting factor under the maximum AGV weight.

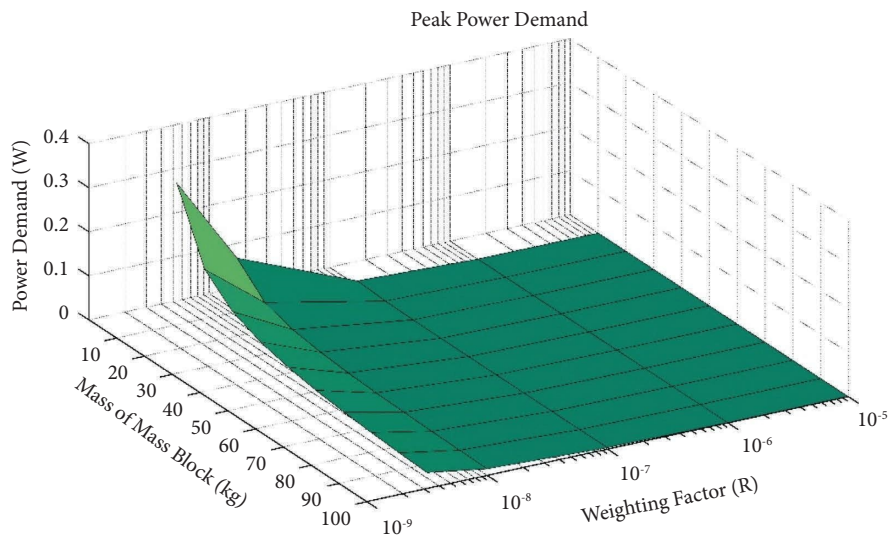


FIGURE 16: Peak power demands with different masses of mass block and active control force weighting factor under the maximum AGV weight.

$x_a = 12.18 \mu\text{m}$. Moreover, the PBIS can suppress the horizontal microvibrations of the tall platform, especially higher frequency responses, as shown in Figure 18, whereas it can amplify the vertical microvibrations of the tall platform at around the vertical natural frequencies of the floor system even though this study does not focus on the assessment of vertical vibration control performance of the tall platform. Moreover, as mentioned earlier, in real-life high-tech

production fabs, there are several complicated gas and fluid pipelines connected between floors and processing tools or platforms. Therefore, the PBIS may not apply to such specific tall platforms, whereas the APMD installed on the top of the tall platform without supplementary damping and spring elements to tune the natural frequency as required by the ATMD could be a feasible and promising approach in precision microvibration control.

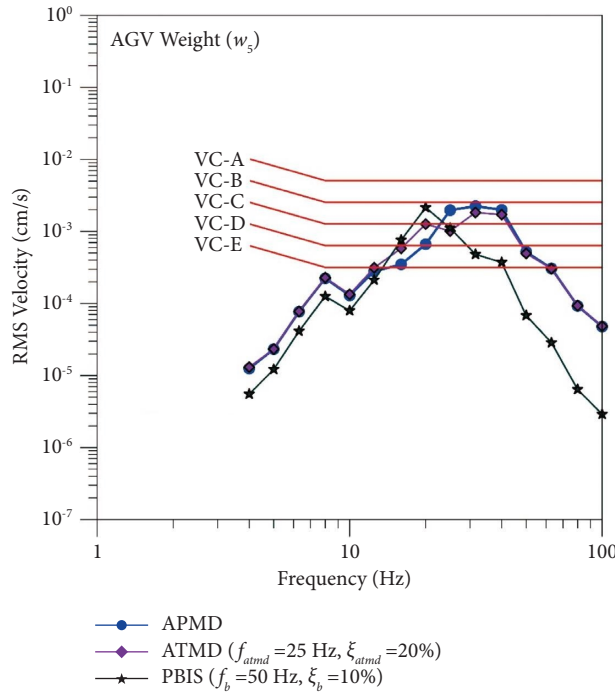


FIGURE 17: Comparison of RMS vibration spectra of the platform implemented with APMD, ATMD, or PBIS under the maximum AGV weight.

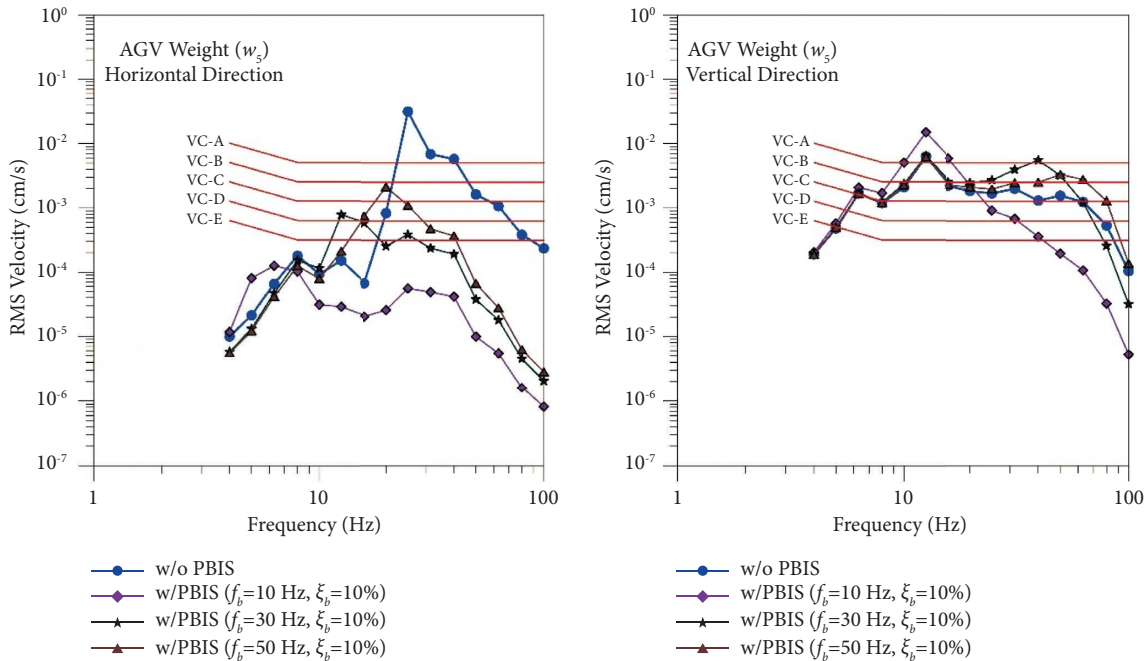


FIGURE 18: Horizontal and vertical RMS vibration spectra of the platform with and without PBIS under the maximum AGV weight.

5. Concluding Remarks

The present study assessed the AGV-induced microvibration control performance of tool platforms using the APMD. The tool platform with a mass of 3000 kg and a fundamental

frequency of 25 Hz was mounted on a three-span continuous floor (or beam) model of an LCD fab. The optimal feedback gain factors of the APMD that were derived based on the direct output feedback control algorithm were numerically obtained using an iterative procedure. Dynamic time history and one-

third octave band spectrum analyses of the proposed beam-platform model under the action of different AGV moving forces generated by the MKT-PSD functions were performed. The numerical simulation results revealed that the floor microvibrations exceed the desired VC-B level and that the tool platform microvibrations induced by the base rotation excitation without APMD generally exceed the VC-A level regardless of the AGV weight. Significant reductions of over 90% on the tool platform microvibrations under the AGV movements could be achieved if the platform is implemented with the APMD considering the appropriate mass ($m_a = 50$ kg) of the mass block and weighting factor ($R = 10^{-8.5}$) of the active control force. Moreover, the APMD could effectively suppress the platform microvibrations under the maximum AGV weight ($w_5 = 21582$ N) to satisfy the allowable VC-B level by demanding less active control force (38.74 N), stroke (18.16 μ m), and applied voltage (242.99 V), which can now be easily realized using the piezoelectric stack actuators. In addition, comparisons of the microvibration control performance of the tall platform implemented with APMD, ATMD, or PBIS under the maximum AGV weight have been performed. Simulation results showed that all three control or isolation schemes can suppress the horizontal microvibrations of the tall platform below the allowable VC-B level. The APMD consisting of piezoelectric stack actuator and mass block without auxiliary spring and damping devices exhibits comparable control performance to the ATMD. Conversely, although the PBIS could further suppress horizontal microvibrations of the tall platform at a higher frequency range, it could amplify vertical microvibrations around the vertical natural frequencies of the floor system. Moreover, due to complex gas and fluid pipelines connected between floors and processing tools or platforms in real-life high-tech production fabs, it would be a challenge to realize vibration isolation by installing the PBIS underneath the platform base. Therefore, the simulated results obtained herein suggest the feasibility of using the proposed APMD to realize the horizontal microvibration control of such specific tall platforms subjected to the AGV-induced floor vibrations with larger intensity and broader bandwidth in LCD fabs. Consequently, future studies may focus on the development of innovative active microvibration control systems and base isolation devices (hybrid control schemes) to suppress both the vertical and horizontal microvibrations of tall platforms under AGV movements.

Data Availability

The data used to support the findings of this study are available from the corresponding author upon reasonable request.

Conflicts of Interest

The authors declare that they have no conflicts of interest.

Acknowledgments

This research was supported by the Fujian Provincial Department of Science & Technology (Project no. 2017J01495), Xiamen University of Technology (Project no. YKJ17008R),

China, Ningbo Science and Technology Bureau under grant no. 2023J189, and Seed Funding from University of Nottingham Ningbo China under grant no. RESI202209001.

References

- [1] D. Nazzal, *Analytical approach to estimating AMHS performance in 300mm Fabs*, Ph.D. thesis, School of Industrial and Systems Engineering, Georgia Institute of Technology, Atlanta, Georgia, 2006.
- [2] C. L. Lee, Y. P. Wang, and R. K. L. Su, "A study on AGV-induced floor micro-vibration in TFT-LCD high technology fabs," *Structural Control and Health Monitoring*, vol. 19, no. 3, pp. 451–471, 2012.
- [3] C. L. Lee, Y. P. Wang, and R. K. L. Su, "Assessment of vibrations induced in factories by automated guided vehicles," *Proceedings of the Institution of Civil Engineers-Structures and Buildings*, vol. 166, no. 4, pp. 182–196, 2013.
- [4] S. H. Ju, H. H. Kuo, S. W. Yu, and S. H. Ni, "Investigation of vibration induced by moving cranes in high-tech factories," *Journal of Low Frequency Noise, Vibration and Active Control*, vol. 39, no. 1, pp. 84–97, 2020.
- [5] M. Y. Hu, Y. Lou, J. G. Nie, L. Chen, S. Dou, and W. Huang, "Method for analyzing influence of OHS transport system on micro-vibration of VLSI structure," *Journal of Hefei University of Technology*, vol. 39, no. 6, pp. 812–817, 2016.
- [6] C. G. Gordon, "Generic criteria for vibration sensitive equipment," *SPIE Proceedings*, vol. 1619, pp. 71–85, 1999.
- [7] J. N. Yang and A. K. Agrawal, "Protective systems for high-technology facilities against microvibration and earthquake," *Structural Engineering & Mechanics*, vol. 10, no. 6, pp. 561–575, 2000.
- [8] Y. L. Xu and A. X. Guo, "Microvibration control of coupled high tech equipment-building systems in vertical direction," *International Journal of Solids and Structures*, vol. 43, no. 21, pp. 6521–6534, 2006.
- [9] X. J. Hong, S. Zhu, and Y. L. Xu, "Three-dimensional vibration control of high-tech facilities against earthquakes and microvibration using hybrid platform," *Earthquake Engineering & Structural Dynamics*, vol. 39, no. 6, pp. 615–634, 2010.
- [10] T. C. Pan, A. Mita, and J. Li, "Vehicle-induced floor vibrations in a multistory factory building," *Journal of Performance of Constructed Facilities*, vol. 15, no. 2, pp. 54–61, 2001.
- [11] C. L. Lee, Y. P. Wang, R. K. L. Su, and Y. T. Chen, "Fragility analysis of floor micro vibrations induced by internal vehicles in high technology factories," *Structures*, vol. 40, pp. 679–692, 2022.
- [12] N. Jalili, *Piezoelectric-Based Vibration Control: From Macro to Micro/Nano Scale Systems*, Springer Science Business Media, LLC, New York, NY, USA, 2010.
- [13] C. C. Liu, X. J. Jing, S. Daley, and F. M. Li, "Recent advances in micro-vibration isolation," *Mechanical Systems and Signal Processing*, vol. 56–57, pp. 55–80, 2015.
- [14] G. Song, V. Sethi, and H. N. Li, "Vibration control of civil structures using piezoceramic smart materials: a review," *Engineering Structures*, vol. 28, no. 11, pp. 1513–1524, 2006.
- [15] T. Kamada, T. Fujita, T. Hatayama et al., "Active vibration control of flexural-shear type frame structures with smart structures using piezoelectric actuators," *Smart Materials and Structures*, vol. 7, no. 4, pp. 479–488, 1998.
- [16] H. Hora, M. Yasuda, T. Osako et al., "Feasibility study of active micro-vibration control system using piezoelectric actuators for floor structure of precision manufacturing

- facilities,” in *Proceedings of the 14th World Conference on Earthquake Engineering*, Beijing, China, October 2008.
- [17] S. Etedali, M. R. Sohrabi, and S. Tavakoli, “Optimal PD/PID control of smart base isolated buildings equipped with piezoelectric friction dampers,” *Earthquake Engineering and Engineering Vibration*, vol. 12, no. 1, pp. 39–54, 2013.
- [18] Y. J. Fan, P. C. Zhao, Z. A. Guo, and B. S. Yu, “Dynamic mechanical properties of variable friction damper based on new piezoelectric ceramic tubular actuator,” *Journal of Materials Research and Technology*, vol. 9, no. 5, pp. 10909–10915, 2020.
- [19] H. Vestad and M. Steinert, “A low-cost vibration isolation chamber-Making high precision experiments accessible,” *HardwareX*, vol. 11, Article ID e00264, 2022.
- [20] X. L. Yang, H. Wu, B. Chen, S. Z. Kang, and S. L. Cheng, “Dynamic modeling and decoupled control of a flexible Stewart platform for vibration isolation,” *Journal of Sound and Vibration*, vol. 439, pp. 398–412, 2019.
- [21] S. Jiang, J. Z. Wang, S. K. Wang, and W. Shen, “Vibration isolation control performance for an innovative 3-DOF parallel stabilization platform,” *Journal of Mechanical Science and Technology*, vol. 36, no. 7, pp. 3677–3689, 2022.
- [22] C. Fang, “Frequency domain-based analytical framework for seismic performance of viscously damped outrigger systems based on continuous Timoshenko beam theory,” *Journal of Low Frequency Noise, Vibration and Active Control*, vol. 42, no. 3, pp. 1137–1161, 2023.
- [23] C. Fang, “Applicability of damped outrigger systems using Timoshenko beam theory,” *International Journal of Structural Stability and Dynamics*, vol. 22, no. 6, Article ID 2250076, 2022.
- [24] C. J. Fang, B. F. Spencer, J. Q. Xu, P. Tan, and F. L. Zhou, “Optimization of damped outrigger systems subject to stochastic excitation,” *Engineering Structures*, vol. 191, pp. 280–291, 2019.
- [25] G. L. Lin, C. C. Lin, L. Y. Lu, and Y. B. Ho, “Experimental verification of seismic vibration control using a semi-active friction tuned mass damper,” *Earthquake Engineering & Structural Dynamics*, vol. 41, no. 4, pp. 813–830, 2012.
- [26] S. Y. Chu, L. Y. Lu, and S. W. Yeh, “Real-time hybrid testing of a structure with a piezoelectric friction controllable mass damper by using a shake table,” *Structural Control and Health Monitoring*, vol. 25, no. 3, Article ID e2124, 2018.
- [27] C. Q. Chen and G. Chen, “Shake table tests of a quarter-scale three-storey building model with piezoelectric friction dampers,” *Structural Control and Health Monitoring*, vol. 11, no. 4, pp. 239–257, 2004.
- [28] G. Chen and C. Q. Chen, “Semiactive control of the 20-story benchmark building with piezoelectric friction dampers,” *Journal of Engineering Mechanics*, vol. 130, no. 4, pp. 393–400, 2004.
- [29] J. Pardo-Varela and J. C. de la Llera, “A semi-active piezoelectric friction damper,” *Earthquake Engineering & Structural Dynamics*, vol. 44, no. 3, pp. 333–354, 2015.
- [30] T. L. Wang, X. Zhang, K. Li, and S. X. Yang, “Mechanical performance analysis of a piezoelectric ceramic friction damper and research of its semi-active control strategy,” *Structures*, vol. 33, pp. 1510–1531, 2021.
- [31] C. L. Lee, R. K. L. Su, and Y. P. Wang, “AGV-induced floor micro-vibration assessment in LCD factories by using a regressional modified Kanai-Tajimi moving force model,” *Structural Engineering & Mechanics*, vol. 45, no. 4, pp. 543–568, 2013.
- [32] L. L. Chung, L. Y. Wu, and T. G. Jin, “Acceleration feedback control of seismic structures,” *Engineering Structures*, vol. 20, no. 1-2, pp. 62–74, 1998.
- [33] Y. P. Wang, C. L. Lee, and K. M. Chen, “Seismic structural control using a novel high-performance active mass driver system,” *Earthquake Engineering & Structural Dynamics*, vol. 29, no. 11, pp. 1629–1646, 2000.
- [34] Y. P. Wang, W. H. Liao, and C. L. Lee, “A state-space approach for dynamic analysis of sliding structures,” *Engineering Structures*, vol. 23, no. 7, pp. 790–801, 2001.
- [35] L. L. Chung, Y. P. Wang, and C. L. Lee, “The theory and analysis of micro-vibration measurement data for high-tech facilities,” *Structural Engineering*, vol. 18, no. 2, pp. 47–72, 2003.
- [36] A. K. Chopra, *Dynamics of Structures: Theory and Applications to Earthquake Engineering*, Pearson Education, New Jersey, NJ, USA, fourth edition, 2012.
- [37] M. Shinozuka, “Simulation of multivariate and multidimensional random processes,” *Journal of the Acoustical Society of America*, vol. 49, no. 1B, pp. 357–368, 1971.